Isokinetic analysis of nanocrystallization in an Al–Nd–Ni amorphous alloy

2005 J. Phys.: Condens. Matter 17 4897

(http://iopscience.iop.org/0953-8984/17/32/004)

INSTITUTE OF PHYSICS PUBLISHING JOURNAL OF PHYSICS: CONDENSED MATTER

J. Phys.: Condens. Matter **17** (2005) 4897–4910 doi:10.1088/0953-8984/17/32/004

Isokinetic analysis of nanocrystallization in an Al–Nd–Ni amorphous alloy

D Jacovkis, J Rodriguez-Viejo and M T Clavaguera-Mora

Grup de Física de Materials I, Departament de Física, Universitat Autònoma de Barcelona, 08193-Bellaterra, Spain

E-mail: david@vega.uab.es and mtmora@vega.uab.es

Received 21 December 2004, in final form 26 June 2005
Published 29 July 2005
Online at stacks.iop.org/JPhysCM/17/4897

Abstract

The nanocrystallization process, promoted in an amorphous alloy with nominal composition $Al_{89}Nd_7Ni_4$ by annealing (∼10 min) at temperatures between 480 and 530 K (primary crystallization interval), results in the development of a distribution of primary nanocrystalline particles, with sizes below 10 nm. In the initial steps the nanocrystallization process was found to be controlled by nucleation and diffusion-controlled growth, which is then gradually slowed down by the change in composition of the disordered matrix (soft impingement regime). The kinetics of the process have been explored by the analysis of differential scanning calorimetry (DSC) and x-ray diffraction (XRD) data. We have used the *master curve* method, based on the isokinetic hypothesis, to analyse the calorimetric data, and XRD patterns were used to estimate the mean grain size in the nanocrystalline phase.

1. Introduction

Nanocrystalline materials have given rise to great interest in recent years, mainly due to the improved properties they present with respect to conventionally structured materials [1–12], including mechanical strength, toughness, corrosion and creep resistance. In most cases the final properties critically depend on microstructural parameters [13] (grain size and shape, size distribution), and consequently much effort has been devoted to microstructure control techniques [14].

The present work is part of a study on the nanocrystallization process in Al-based amorphous alloys obtained by melt spinning. Its aim is to investigate the mechanisms controlling the primary crystallization in the $Al_{89}Nd_7Ni_4$ amorphous alloy. This is a thermally activated process that can be typically separated into two different steps: nucleation and grain growth. In multicomponent systems, primary crystallization is usually controlled by the diffusion of solute atoms, and is followed by the precipitation of intermetallic phases at higher temperatures. In several Al-rich amorphous alloys, partial nanocrystallization of the

α-Al phase can be promoted by annealing at relatively low temperatures (between 400 and 500 K). The result of this process is usually a dispersion of α-Al particles embedded in the solute-rich amorphous phase.

The main contribution to fulfil this objective is the introduction of the recently developed *master curve* method for the analysis of kinetic data. Previous studies on Al-based amorphous alloys show that the as-prepared melt-spun samples can either contain quenched-in crystalline embryos [8, 12], or present thermally activated nucleation. The growth of α-Al is diffusion limited, and soft impingement very soon becomes the controlling mechanism [15]. One key tool that may be used to obtain these results is the master curve method introduced for the analysis of kinetic data [16]. In the present work such a method is further explored and developed. A new representation, equivalent to the widely used *Avrami plots*, is proposed, using only continuous heating DSC traces. The analysis is focused on the calorimetric data, the procedure to obtain the master curve and the determination of the activation energy and local Avrami exponent.

2. Experimental techniques

The analysed samples were kindly provided by Professor A Inoue, from Tohoku University, Sendai. They were prepared by melt spinning from a melt with chemical composition $Al_{89}Nd_7Ni_4$. The resulting ribbons, less than 50 μm thick, were cut in small pieces in order to improve thermal contact with the calorimeter.

The calorimetric measurements were performed using a Perkin-Elmer DSC7 calorimeter in a pure Ar atmosphere. The thermal lag correction and temperature/enthalpy calibrations were performed with standard In and Zn samples for each heating rate used (between 20 and 80 K min^{-1}).

Structural information was acquired by x-ray diffraction (XRD) in a Phillips X'PERT diffractometer with conventional Bragg–Brentano geometry, using monochromatic Cu Kα radiation. Scans were taken over a 2θ angle range of 20°–80°, with a step of 0.03°.

Samples explored by XRD after a heat treatment were prepared in the DSC7 calorimeter using a heating rate of 80 K min^{-1}.

3. Experimental results

3.1. X-ray diffraction

3.1.1. Grain size estimation. Grain size is a critical parameter for the properties of any nanocrystalline material. We used conventional XRD data to estimate the mean grain size of the primary phase on samples with different degrees of crystallization. Partial crystallization was attained by previous annealing for 10 min at different temperatures. For a given temperature (i.e., a given degree of nanocrystallization) the analysis proceeded as follows:

The experimental pattern obtained from an as-prepared sample, assumed to be fully amorphous, is fitted by a polynomial function in the angular interval considered (usually the 30°–50° range in 2θ). This numerical fit is then used to subtract the contribution of the amorphous phase from the experimental pattern of the partially crystallized sample under study. The pattern obtained after subtraction corresponds only to the nanocrystalline phase.

The resulting diffraction pattern is finally fitted using the Debye formula in discrete form for the intensity of coherent scattering:

$$I(q) = f^2(q) \sum_{i,j} \frac{\sin\left(q \cdot r_{ij}\right)}{q \cdot r_{ij}}, \tag{1}$$

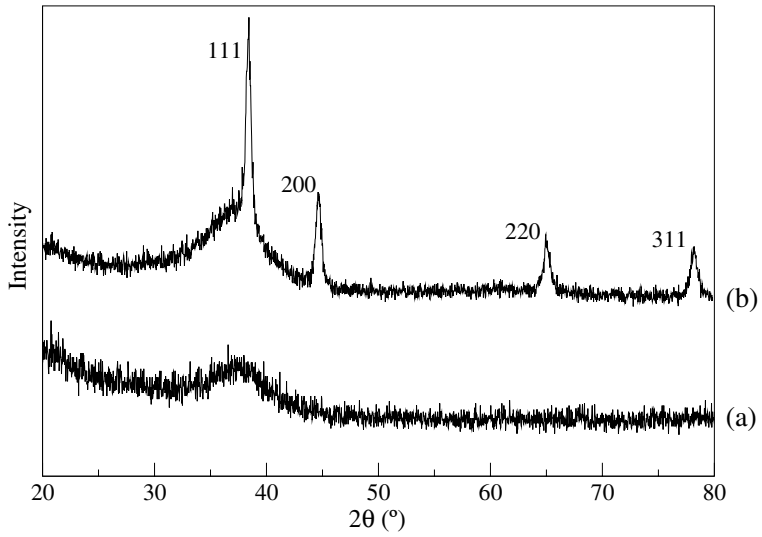

Figure 1. XRD patterns of an as-quenched $Al_{89}Nd_7Ni_4$ ribbon (a), showing a broad peak at 38°, characteristic of amorphous alloys, and of a sample annealed at 573 K for 10 min (b), with the indexing of α-Al peaks.

where

$$q = \frac{4\pi}{\lambda}\sin(\theta), \tag{2}$$

f is the atomic scattering factor for Al atoms, r_{ij} is the distance between atoms i and j, and the sums are over all the Al atoms. This procedure can be applied due to the lack of orientation of the nanocrystals, that allows us to apply equation (1) as if the sample was powder. To simplify the calculations we assume that all grains are spherical and have the same size.

Since the contribution of the amorphous phase has already been subtracted from the experimental pattern, the only fit parameter used in the simulations is the coherent scattering domain size, or grain size, given by the number of atoms considered in equation (1).

3.1.2. XRD results. The XRD patterns obtained from as-quenched ribbons confirm that the samples are amorphous, as shown by the typical broad halo in the diffraction pattern and the absence of sharp crystalline peaks (see figure 1(a)).

After annealing for 10 min at 573 K, several peaks appear in the diffraction pattern. These peaks have been identified as the first diffracting planes in the α-Al crystalline structure, which is the primary phase in this alloy. As shown in figure 1(b), a considerable amount of amorphous phase remains in the sample after primary crystallization. This amorphous phase is enriched in Nd and Ni, since no phases other than the primary precipitate up to this temperature. The width of the peaks suggests nanometric grain sizes in the primary phase. An exhaustive analysis of this data, following the method described in section 3.1.1, supports this observation.

The analysed diffraction patterns were obtained from samples previously annealed for 10 min at 475, 485, 495 and 533 K. The calculated mean grain size in each sample is shown in figure 2, where we can see that grain size stabilizes around 9–10 nm in the samples annealed at the higher temperatures.

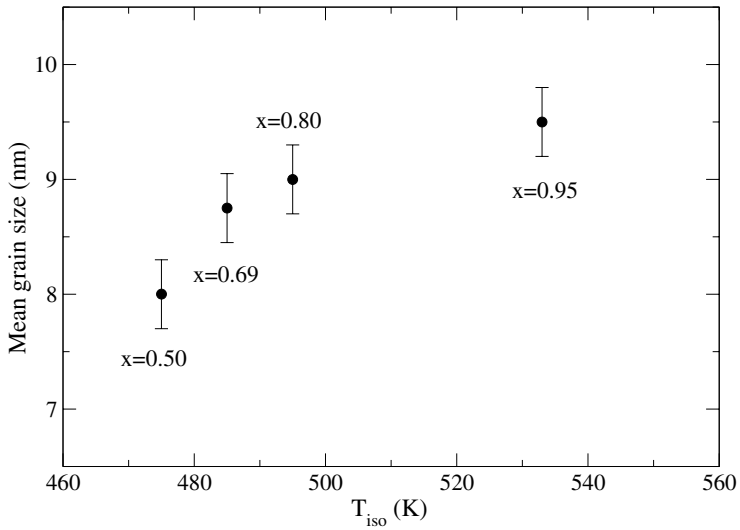

Figure 2. Mean grain size, estimated from XRD and DSC data after 10 min annealing at different temperatures, calculated as described in section 3.1.1. Annotated values of the transformed fraction were estimated from the kinetic function.

3.2. Differential scanning calorimetry

3.2.1. Data analysis: master curve method. The purpose of this method is to isolate the kinetic information that can be obtained from calorimetric data in continuous heating mode. The method was devised to work with several datasets obtained at different heating rates. The analysis of data obtained during linear heating is of great interest, especially in the initial stages of crystallization, since in the isothermal mode some data are always lost in the time required to reach the experimental temperature and system stabilization. In addition, analysis in the linear heating mode is often faster than in the isothermal mode, making it more attractive for industrial applications.

The analysis of DSC data has been widely used to obtain kinetic information of crystallization reactions [17]. Most of these studies rely on the *isokinetic hypothesis* to separate the kinetics of the transformation from its dependence on temperature, assuming that the transformation rate can be described by a differential equation separable in α (transformed fraction) and T (temperature). In the continuous heating regime:

$$\frac{\mathrm{d}\alpha}{\mathrm{d}T} = \frac{1}{\beta}\frac{K(T)}{P(\alpha)}, \tag{3}$$

where β is the heating rate, $K(T)$ is frequently referred to as the *rate constant*, and $P(\alpha)$ is the *kinetic function*, since it depends only on the transformation mechanisms and not on the thermal path.

When dealing with primary crystallization, it is convenient to normalize α to the total primary transformed fraction α_p,

$$x \equiv \frac{\alpha}{\alpha_\mathrm{p}}, \tag{4}$$

so by definition $x = 1$ when $\alpha = \alpha_p$. Determining the value of α_p is not necessary for the present analysis, since x is the partial area under the primary peak in continuous heating mode:

$$x(T) = \frac{\int_{T_{onset}}^{T_{end}} \frac{dQ}{dt} dT}{S}, \tag{5}$$

where T_{onset} and T_{end} are respectively the onset and end temperature of the primary crystallization, S is the total area of the primary peak, and $\frac{dQ}{dt}$ is the calorimetric signal.

Equation (3) can be written in integral form as

$$G(x) \equiv \int_0^x P(x')\,dx' = \frac{1}{\beta}\int_{T_0}^{T} K(T')\,dT'. \tag{6}$$

As can be readily seen in this equation, $G(x)$ does not depend on the thermal path if the reaction is isokinetic. In thermally activated processes, the range of temperatures in which the transformation proceeds is narrow enough to consider that $K(T)$ is Arrhenian, that is,

$$K(T) = \exp\left(\frac{-E_{ap}}{kT}\right), \tag{7}$$

where E_{ap} is the apparent activation energy of primary crystallization and k is the Boltzmann constant.

For any pair of heating rates β_i and β_j we can write, following equations (6) and (7),

$$\frac{1}{\beta_i}\int_{T_0}^{T_i} \exp\left(\frac{-E_{ap}}{kT'}\right) dT' = \frac{1}{\beta_j}\int_{T_0}^{T_j} \exp\left(\frac{-E_{ap}}{kT'}\right) dT', \tag{8}$$

where T_0 is the room temperature. Equations (6) and (8) provide the basis for the development of the *master curve* method. The goal is to obtain an ensemble of transformed datasets that should be identical, i.e., independent of the heating rates under which they were obtained, when equations (3) and (7) are satisfied. According to equation (8) one can transform a calorimetric curve obtained at a given heating rate (β_i) to another heating rate (β_j), finding for every original temperature T_i a transformed temperature T_j that maintains the equality. This transformation ensures that the transformed fraction at the original and transformed temperatures is the same, i.e., $x(T_i;\beta_i) = x(T_j;\beta_j)$. This can be readily seen from equation (6): for a given degree of crystallization, x, $G(x)$ is determined. Moreover, the transformation rate $\frac{dx}{dT}|_j$ is obtained through normalization by

$$\left.\frac{dx}{dT}\right|_j = \frac{\left.\frac{dx}{dT}\right|_i}{C_{ij}}, \tag{9}$$

where

$$C_{ij} = \int_{T_{onset}}^{T_{end}} \left.\frac{dx}{dT}\right|_i dT_j, \tag{10}$$

since

$$\int_{T_{onset}}^{T_{end}} \left.\frac{dx}{dT}\right|_k dT_k = 1, \qquad \text{for } k = i, j. \tag{11}$$

The transformation shown in equation (8) can be applied to every experimental point in a calorimetric curve to obtain an equivalent curve at another heating rate. One can change the heating rate and transform all the experimental points of the calorimetric curve to obtain the equivalent curve for the new heating rate. The method proceeds as follows.

First, we obtain the calorimetric data at different heating rates. In principle any number of curves and heating rates can be used, but it is convenient to choose at least three different

heating rates and two curves at each rate to improve statistics. The heating rates should not differ too much, and should not be too high (say, higher than 80 K min^{-1}), since the isokinetic hypothesis implies that equilibrium is reached at each temperature during heating. The n heat flow curves $[\frac{\mathrm{d}Q}{\mathrm{d}t}|_i, T_i; \beta_i]_n$ are then converted to transformation rate curves $[\,\frac{\mathrm{d}x}{\mathrm{d}T}\big|_i\,, T_i; \beta_i]_n$ by dividing the signal by the total area of the primary peak (see equation (5)).

Once the curves are prepared we obtain a first estimation of the apparent activation energy using the Kissinger method [18]. Then we begin an iterative process with the activation energy as a parameter, varying it in an interval around the first estimate. For each value of the activation energy, all the experimental curves $[\,\frac{\mathrm{d}x}{\mathrm{d}T}\big|_i\,, T_i; \beta_i]_n$ are transformed to *equivalent heating rate* curves $[\,\frac{\mathrm{d}x}{\mathrm{d}T}\big|_j\,, T_j; \beta_j]_n$ using equations (8) and (9).

The n transformed curves $[\,\frac{\mathrm{d}x}{\mathrm{d}T}\big|_j\,, T_j]$ for a fixed heating rate β_j are then averaged, and their dispersion with regard to the average curve $[\,\frac{\mathrm{d}x}{\mathrm{d}T}\big|_{\mathrm{av}}\,, T_{\mathrm{av}}]$ calculated.

If all the previous assumptions hold, the transformed curves will overlap for some value of the apparent activation energy. Obviously the overlap will not be perfect, but the iterative method is designed to find the value of the apparent activation energy that gives the smallest dispersion of the transformed curves with regard to the averaged curve, which we will call the *master curve* $[\,\frac{\mathrm{d}x}{\mathrm{d}T}\big|_{\mathrm{mc}}\,, T_{\mathrm{mc}}]$ at rate β_{mc}.

This method provides at the same time a value of the apparent activation energy and the *kinetic function* $P(x)$. Since the *master curve* method works with all the points of the calorimetric curves, this value of E_{ap} is more reliable than the one obtained with the Kissinger method [18], which considers only one point per curve. Nevertheless, it is worth mentioning that the *master curve* method requires that equations (3) and (7) hold, as normally required for the quantity E_{ap} to have a physical meaning.

According to equation (3), $P(x)$ is obtained from the *master curve* $[\frac{\mathrm{d}x}{\mathrm{d}T}, T_{\mathrm{mc}}]$ by

$$P(x) = \frac{1}{\beta_{\mathrm{mc}}}\left[\frac{\mathrm{d}x}{\mathrm{d}T}\right]^{-1}_{\mathrm{mc}} \exp\left(\frac{-E_{\mathrm{ap}}}{kT'}\right). \tag{12}$$

Note that this result does not depend on our choice of the equivalent heating rate. One last step to obtain the kinetic function consists of changing the temperature dependence of $[\frac{\mathrm{d}x}{\mathrm{d}T}]_{\mathrm{mc}}$ to a dependence on the transformed fraction x. This is done by inverting the $x(T)$ function, that can be calculated by integration of the master curve.

This step allows us to isolate the dependence of the transformation rate on the transformed fraction, making possible the study of the mechanisms controlling the transformation at any temperature (or heating rate) within the isokinetic range. Both the kinetic function $P(x)$ and its integral $G(x)$ can be compared to well established models, like the framework developed by Kolmogorov, Johnson, Mehl and Avrami (KJMA) [19–23]. In this model, the kinetic function can be written as

$$P_{\mathrm{KJMA}}(x) = P_0 \frac{\{-\ln(1-x)\}^{\frac{1-n}{n}}}{n(1-x)}, \tag{13}$$

and its integral

$$G_{\mathrm{KJMA}}(x) = P_0\{-\ln(1-x)\}^{\frac{1}{n}}, \tag{14}$$

where P_0 is a *characteristic time* constant and n is the *Avrami exponent*. This last parameter reflects the mechanisms involved in the transformation [24].

The values of the constants E_{ap} and P_0 can now be expressed in terms of the nucleation and growth rates for the different growth mechanisms. We assume that the nucleation, interface-controlled growth and effective diffusion rates follow Arrhenian laws,

$$I = I_0 \exp\left(-\frac{E_{\mathrm{I}}}{kT}\right), \tag{15}$$

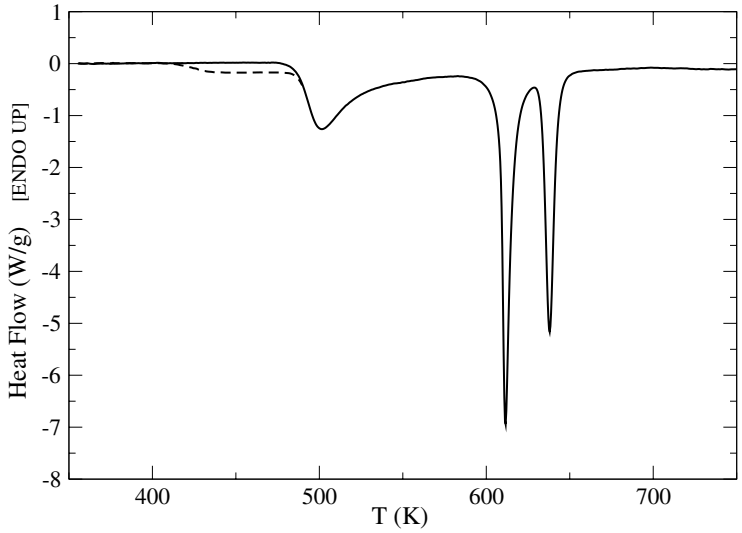

Figure 3. Heat flow during continuous heating of the $Al_{89}Nd_7Ni_4$ sample at 60 K min^{-1}. The dashed line corresponds to an as-prepared sample, while the full line corresponds to a sample where relaxation of the amorphous sample was promoted by previous heating up to 475 K.

Table 1. P_0^{-1} and E_{ap} in terms of the nucleation frequency, the growth rate and the effective diffusion coefficient, in the KJMA framework.

	Avrami exponent n	E_{ap}	P_0^{-1}
Interface-controlled growth, constant nucleation	4	$\frac{E_I + 3E_u}{4}$	$\left\{\frac{\pi}{3} I_0 u_0^3\right\}^{\frac{1}{4}}$
Interface-controlled growth, pre-existing nuclei[a]	3	E_u	$\left\{\frac{4\pi}{3} N u_0^3\right\}^{\frac{1}{3}}$
Diffusion-controlled growth, constant nucleation	5/2	$\frac{2E_I + 3E_D}{5}$	$\left\{\frac{8\pi}{15} I_0\right\}^{\frac{2}{5}} \{2D_0\}^{\frac{3}{5}}$
Diffusion-controlled growth, pre-existing nuclei[a]	3/2	E_D	$\left\{\frac{4\pi}{3} N\right\}^{\frac{2}{3}} \{2D_0\}$

[a] N: density of pre-existing nuclei.

$$u = u_0 \exp\left(-\frac{E_u}{kT}\right), \tag{16}$$

and

$$D = D_0 \exp\left(-\frac{E_D}{kT}\right), \tag{17}$$

where I, u, and D are respectively the nucleation rate, interface-controlled growth rate, and effective diffusion coefficient, E_I, E_u and E_D are the corresponding activation energies, and I_0, u_0 and D_0 are the corresponding pre-exponential factors. If we consider spherical particles growing from negligible dimensions, the different values of n can be interpreted in terms of crystallization mechanisms, as shown in table 1.

3.2.2. DSC results. Figure 3 shows the typical DSC signal obtained during continuous heating of a sample of the $Al_{89}Nd_7Ni_4$ amorphous alloy. Several features of the crystallization

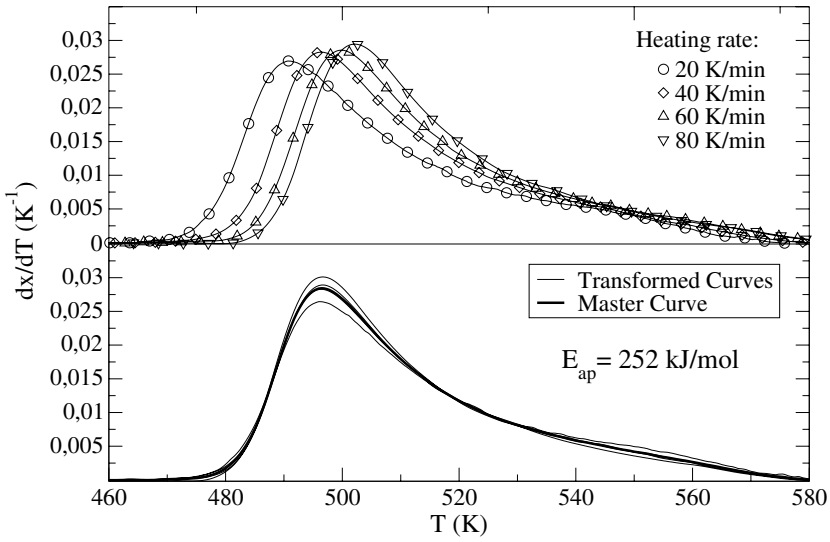

Figure 4. DSC curves corresponding to the primary crystallization, obtained at 20, 40, 60 and 80 K min^{-1}, transformed to an equivalent heating rate of 40 K min^{-1} by the *master curve* method.

process can be appreciated in this figure. The first is a change in the baseline around 410 K, with a negative shift of ∼0.2 W g^{-1}. This change can be associated with relaxation in the amorphous material, as suggested by the fact that previous heating up to 475 K (dashed line in figure 3) removes this baseline shift without modifying the crystallization peak.

At 480 K primary crystallization begins. The peak is markedly asymmetric, as the tail is much longer than the onset. This shape is characteristic of diffusion-controlled growth [1, 7, 11]: solute atoms, rejected from the growing α-Al grains, build up near the interfaces, forming a barrier that has to diffuse away to permit further growth.

The end of the primary crystallization peak overlaps with the beginning of the secondary precipitation, separated in two sharp peaks.

We have performed the *master curve* analysis on continuous heating data obtained at 20, 40, 60 and 80 K min^{-1}. Figure 4 shows the transformation rate curves obtained at various heating rates (upper figure), and the transformed curves at an equivalent heating rate of 40 K min^{-1}, together with the master curve obtained by averaging them (bottom figure). With this procedure, an apparent activation energy of 2.61 eV/atom was obtained. The initial estimation of E_{ap}, obtained by the Kissinger method, was 2.71 eV/atom. The good overlap of the transformed curves supports the use of the isokinetic hypothesis.

Once the master curve has been calculated, we can extract the $P(x)$ function in order to study the kinetics of the primary crystallization. Figure 5 shows $P(x)$, obtained by applying equation (12) to the master curve shown with a bold line in the bottom graph of figure 4.

In order to compare the experimental $P(x)$ function to the growth models described in table 1, tentative fits of the asymptotic behaviour at the beginning and end of the transformation with fixed values of the Avrami exponent are also plotted in the figure. The values used for the asymptotic plots are shown in table 2.

Equivalently, we obtained by integration the experimental $G(x)$ function (see equation (6)), extrapolating to the onset of the transformation the asymptotic behaviour observed experimentally for $5 \times 10^{-3} \leqslant x \leqslant 5 \times 10^{-2}$ (see table 2). The result is shown in

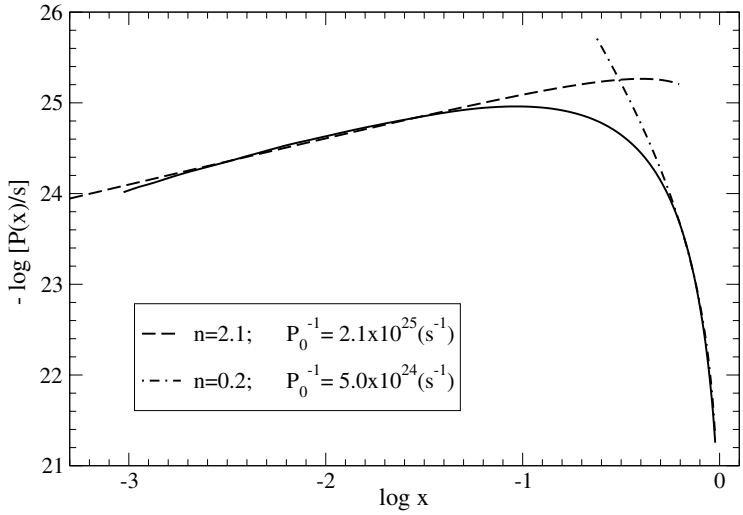

Figure 5. *Kinetic function* obtained from continuous heating data (full line). Asymptotic behaviour explored with the KJMA function (equation (13)): the initial asymptotic fit is valid up to $x \lesssim 0.05$, and the final one is valid for $x \gtrsim 0.6$.

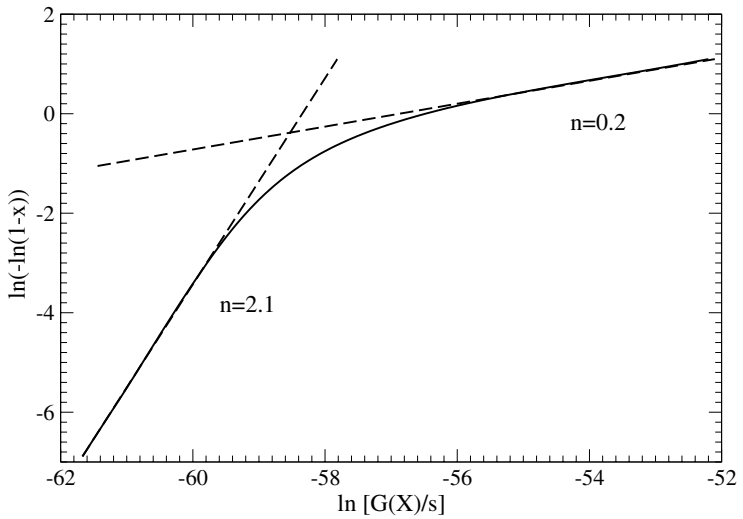

Figure 6. $G(x)$ function obtained by integration of $P(x)$ (full line). The dashed lines correspond to the asymptotic fits of the $P(x)$ function. The slope of the dashed lines is n (see equation (14)).

Table 2. Parameter values used in the asymptotic fits of the experimental $P^{-1}(x)$ function.

Range of fit	P_0^{-1} (s^{-1})	n
$5 \times 10^{-3} \leqslant x \leqslant 5 \times 10^{-2}$	2.2×10^{25}	2.1
$6 \times 10^{-1} \leqslant x \leqslant 9.55 \times 10^{-1}$	5.0×10^{24}	0.2

figure 6, which is equivalent to the widely used *Avrami plots* (plots of $\ln(-\ln(1-x))$ versus logarithm of isothermal time), but obtained from continuous heating data: here we use $G(x)$

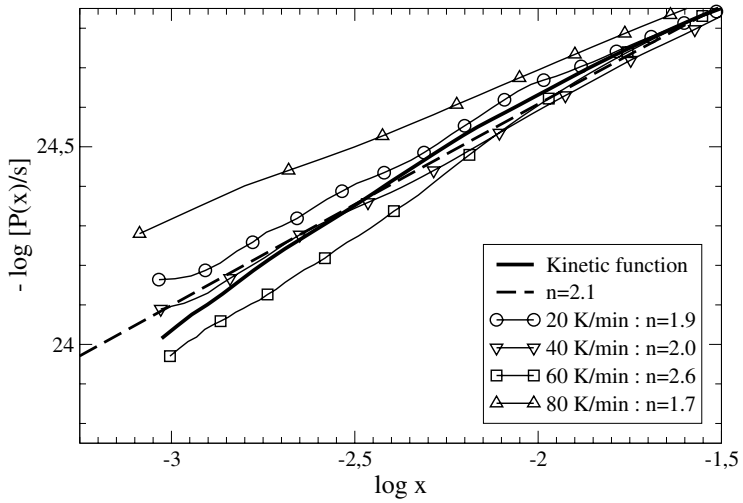

Figure 7. Low-fraction detail of the kinetic fuction, showing the transformed datasets at each heating rate and the corresponding values of the Avrami exponent.

instead of time, but from equation (14) we can see that the slope of the plot is the Avrami exponent.

In order to check the deviation of the transformed datasets with respect to the master curve, we plotted the kinetic function $P(x)$ obtained from the master curve and from each of the transformed datasets. The result is shown in figure 7 for small fractions, the region where the present study is focused. It is important to note that there is no systematic deviation of the curves depending on heating rate, in agreement with the isokinetic hypothesis. There is however an important deviation of the high heating rate curves with respect to the master curve. This deviation can be evaluated by fitting the transformed datasets by an Avrami exponent, also shown in the figure, and is a consequence of the instrumental error associated with the higher heating rates. The figure shows clearly that the deviation is small for the curves obtained at lower heating rates. In future applications of this method care will be taken to use datasets obtained at heating rates below 40 K min^{-1}.

4. Discussion

The experimental DSC and XRD results presented in this paper show that primary crystallization in the $Al_{89}Nd_7Ni_4$ amorphous alloy is a thermally activated process. We have demonstrated that the isokinetic hypothesis is suitable for the analysis of the DSC data, and the good overlap of the transformed curves is indicative of a constant apparent activation energy. The value obtained for the apparent activation energy is 2.61 eV/atom.

Grain size estimations from XRD data (see figure 2) reveal that, as annealing temperature increases from 475 to 495 K, grain size increases from 8 to 9 nm, for an annealing time of 10 min, and stabilizes around 10 nm above 500 K. The transformed fraction under isochronal annealing may be evaluated from the value of $G(x)$ plotted in figure 6, since from equation (6) we have

$$G(x) = \frac{1}{\beta}\int_{T_0}^{T_{\mathrm{iso}}} \exp\left(-\frac{E_{\mathrm{ap}}}{kT}\right) \mathrm{d}T + t_{\mathrm{iso}} \cdot \exp\left(-\frac{E_{\mathrm{ap}}}{kT_{\mathrm{iso}}}\right), \tag{18}$$

Table 3. Values of x and $G(x)$ after 10 min anneals, calculated from the kinetic function. Also shown is the fraction transformed during heating (x_h) and the corresponding equivalent isothermal times (t_{eq}).

T (K)	x_h	t_{eq} (s)	$G(x)$ (s)	x
475	0.0005	5.8	1.26×10^{-25}	0.50
485	0.009	6.0	4.68×10^{-25}	0.69
495	0.1	6.2	1.65×10^{-24}	0.81
533	0.8	7.0	1.30×10^{-22}	0.97

where in this case $\beta = 80$ K min^{-1}. The first term in the right-hand side of this equation accounts for the heating ramp previous to isochronal annealing. Since $G(x)$ was obtained from $P(x)$ we can calculate $t_{iso}(x)$ for a given temperature from equation (18), and since $t_{iso}(x)$ is a monotonic function it can be inverted to obtain $x(t_{iso})$. The value of $G(x)$ obtained for the heating ramp can be used to obtain the fraction transformed during heating, x_h, and the *equivalent isothermal time* t_{eq}, i.e., the time needed at the isothermal temperature to transform the same fraction of sample that precipitates during the ramp.

Table 3 shows the estimated values of x and $G(x)$ for 10 min isothermal anneals, at the temperatures explored in section 3.1.2, together with the fraction transformed during heating (x_h) and the *equivalent isothermal time* (t_{eq}). As can be seen from the table, the fraction transformed during heating is important at the higher temperatures: heating from room temperature up to 533 K at 80 K min^{-1} promotes the precipitation of 80% of the final volume occupied by the primary phase. If heating were instantaneous, this fraction would be achieved in just 7 s of isothermal annealing at 533 K. These data may be compared to the grain size estimations obtained from x-ray diffraction, and suggest that the mean grain size increase observed between 475 and 500 K is mainly due to the crystallization fraction increase, whereas it reaches saturation at the latest stages of the transformation.

Fits of the $P(x)$ function obtained from DSC data (see figure 5) indicate that the initial stages of the primary precipitation (for $x \lesssim 0.05$) can be described within the KJMA framework with a kinetic exponent $n = 2.1$. Although the interpretation of this coefficient is not straightforward, this value lies between 3/2 (diffusion-controlled growth of pre-existing grains) and 5/2 (diffusion-controlled growth with constant nucleation rate), and can be identified with grain growth controlled by diffusion combined with a decreasing nucleation rate. The process has been modelled with a decreasing nucleation rate, I_{soft}, where nuclei have negligible critical size, and a soft diffusion growth rate, $\left(\frac{dR}{dt}\right)_{soft}$, respectively of the form

$$I_{soft} = I_0 \exp\left(-\frac{E_I}{kT}\right) \cdot (1 - x) \tag{19}$$

$$R\left(\frac{dR}{dt}\right)_{soft} = D_0 \exp\left(-\frac{E_D}{kT}\right) \cdot (1 - x), \tag{20}$$

with $\frac{2E_I+3E_D}{5} = E_{ap}$. These equations, though empirical, reproduce qualitatively the continuous decay of both nucleation frequency (due to the decrease of supersaturation of the disordered matrix) and the concentration gradient ahead of the interface (due to soft impingement between grains). The kinetic function $P(x)$ and the transformed fraction x are calculated using the extended fraction, x_{ext}, through the following equations:

$$P^{-1}(x) = \beta \exp\left(\frac{E_{ap}}{kT}\right)\frac{dx}{dT} \tag{21}$$

$$x = 1 - \exp(-x_{ext}), \tag{22}$$

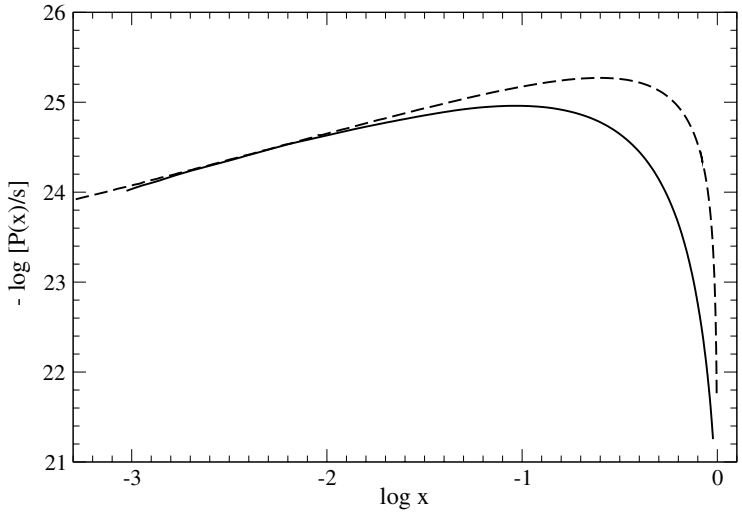

Figure 8. Comparison between the experimental kinetic function $P(x)$ (full line) and the modelled one (dashed line).

with

$$x_{\text{ext}} = \frac{4\pi}{3\beta}\int_{T_0}^{T} I_{\text{soft}}(T')\{R(T',T)\}^3\,\mathrm{d}T' \tag{23}$$

$$\{R(T',T)\}^2 = \frac{1}{\beta}\int_{T'}^{T} 2D_0\exp\left(-\frac{E_{\text{D}}}{kT''}\right)(1-x\{T''\})\,\mathrm{d}T'', \tag{24}$$

and

$$\frac{\mathrm{d}x_{\text{ext}}}{\mathrm{d}T} = \frac{4\pi}{\beta}\int_{T_0}^{T} I_{\text{soft}}(T')\{R(T',T)\}^2\left(\frac{\mathrm{d}R}{\mathrm{d}t}\right)_{\text{soft}}\mathrm{d}T'. \tag{25}$$

The results of the calculation for $\{\frac{8\pi}{15}I_0\}^{\frac{2}{5}}\{2D_0\}^{\frac{3}{5}} = 3.6\times10^{25}\ \text{s}^{-1}$ are shown in figure 8. A simple modelling of the decrease of both nucleation rate and effective diffusion in primary crystallization, such as the one described above, is able to reduce the Avrami exponent at the onset of the transformation, from the *ideal* value of 5/2 to values close to those observed experimentally ($\sim$2.1). Also, the experimental value of P_0 ($2.1\times10^{25}\ \text{s}^{-1}$) is close to the *ideal* one ($3.6\times10^{25}\ \text{s}^{-1}$). However, such a simple model does not reproduce the observed behaviour for $x \gtrsim 2\%$. This is most probably due to the simplicity of the proposed model.

In the final stages of nanocrystallization ($x \gtrsim 0.6$), the experimental kinetic function $P(x)$ may be approached by an Avrami function with $n = 0.2$. Values of this parameter smaller than unity have been previously related to soft impingement processes [15], where grain growth is kinetically slowed down, and eventually inhibited, by the change of concentration in the untransformed region. This image is consistent with the data presented above: after an initial growth stage controlled by hard diffusion, a solute barrier forms outside the interfaces due to the rejection of solute atoms by the primary grains. From this moment, the limiting factor for growth is the movement of that barrier, which, in turn, is affected by the mean concentration of the amorphous matrix. Before geometric impingement between primary grains occurs, the diffusion fields associated with these grains overlap, gradually slowing their growth. This gradually decreasing growth rate is clearly shown by the long tails of the DSC curves obtained in the continuous heating mode, as in figure 3. Due to this effect the mean grain size after

primary crystallization barely reaches 10 nm, with nanocrystals embedded in a solute-enriched amorphous matrix. As mentioned before, this kind of microstructure is attractive for several applications.

No clear end of primary crystallization is observed, since the tail of the first DSC peak overlaps with the onset of the second one. Further growth of primary particles, kinetically inhibited by soft impingement, becomes possible again due to the change in the composition of the matrix caused by the precipitation of new phases. This behaviour has been observed in similar Al-based amorphous alloys.

The analysis of the nanocrystallization process in the $Al_{89}Nd_7Ni_4$ alloy can be compared with a recently published study of a similar alloy [16], with composition $Al_{87}Ni_7Cu_3Nd_3$. The main compositional difference between both alloys is the presence of a small amount of Cu in the latter. The master curve analysis applied to the $Al_{87}Ni_7Cu_3Nd_3$ alloy led to a significantly lower value of the apparent activation energy of nanocrystallization: 1.09 eV/atom. The onset temperature of nanocrystallization in this case was also lower, 400 K when heating at 60 K min^{-1}, while in the present study this value is 480 K.

In the $Al_{87}Ni_7Cu_3Nd_3$ alloy, the main mechanism controlling primary crystallization was found to be the diffusion-controlled growth of a high density (around 10^{17} grains cm^{-3}) of pre-existing grains, and no evidence of thermally activated nucleation was found. In the present study the composition of the alloy is richer in Nd, poorer in Ni, and does not contain Cu, but the preparation method was the same for both alloys. Consequently, differences in the primary crystallization process can be attributed to the compositional changes. Experimental evidence suggests that the high activation energy, together with the increase in the onset temperature, reflect an additional energetic cost for the formation of the primary phase. The activation energies of grain growth, associated with the diffusion of the solute atoms, can be assumed to be similar in both alloys, maybe slightly higher in the present alloy due to the higher concentration of the heaviest solute species, Nd. Therefore, the observed increase of around 1.5 eV/atom in the apparent activation energy can be identified with thermally activated nucleation. This conclusion suggests that a small amount of Cu can critically affect the rapid solidification process, promoting the nucleation of primary grains during quenching.

5. Conclusions

The analysis of DSC data obtained during continuous heating in the temperature range corresponding to primary crystallization was performed using the *master curve* method. This analysis led to a value for the apparent activation energy of nanocrystallization, $E_{ap} = 2.61$ eV/atom.

The method was also used to obtain the empirical kinetic function $P(x)$, and its integral $G(x)$. These functions contain information on the nanocrystallization process. We demonstrated that a very useful representation, equivalent to the *Avrami plot*, can be obtained from continuous heating data using the $G(x)$ function. The analysis of these functions within the KJMA framework has provided us with some insight into the mechanisms controlling the initial and final stages of primary crystallization: the process begins with the thermally activated nucleation of α-Al nuclei, and the subsequent diffusion-controlled growth of these nuclei. The growth rate is gradually slowed down by the overlap of the diffusion fields associated with each of the growing grains, and the growth mode becomes controlled by this *soft impingement*. The nanocrystals continue growing at a very slow rate, until the secondary phase precipitates.

Isothermal annealing for 10 min at several temperatures near the onset of primary crystallization leads to a high density (10^{17} grains cm^{-3}) of α-Al nanocrystals with mean sizes below 10 nm, formed by nucleation and growth from the amorphous phase.

Acknowledgments

This work was supported by the Comisión Interministerial de Ciencia y Tecnología (projects No MAT2001-2532 and MAT2003-8271-C02-01) and the Comissió Interdepartamental de Ciència i Tecnologia (Project No. 2001SGR-00190). DJ is grateful for the financial support granted by the Universitat Autònoma de Barcelona.

References

[1] Inoue A, Nakazato K, Kawamura Y and Masumoto T 1994 *Mater Sci. Eng.* A **179** 654
[2] Hono K, Zhang Y, Tsai A P, Inoue A and Sakurai T 1995 *Scr. Metall. Mater.* **32** 191
[3] Inoue A and Kimura H 2001 *J. Light Met.* **1** 31
[4] Kim Y K, Soh J R, Kim D K and Lee H M 1998 *J. Non-Cryst. Solids* **242** 122
[5] Zhang L, Chen K, Huang X, Wu Y and Bian X 2001 *J. Phys.: Condens. Matter* **13** 5947
[6] Poon S J, Shiflet G J, Guo F Q and Ponnambalam V 2003 *J. Non-Cryst. Solids* **317** 1
[7] Clavaguera N, Diego J A, Clavaguera-Mora M T and Inoue A 1995 *Nanostruct. Mater.* **6** 485
[8] Tsai A A, Kamiyama K, Kawamura Y and Inoue A 1997 *Acta Mater.* **45** 1477
[9] Ye F and Lu K 2000 *J. Non-Cryst. Solids* **262** 228
[10] Jiang X Y, Zhong Z C and Greer A L 1997 *Mater. Sci. Eng.* A **226–228** 789
[11] Allen D R, Foley J C and Perepezko J H 1998 *Acta Mater.* **46** 431
[12] Hong S J, Warren P J and Chun B S 2001 *Mater. Sci. Eng.* A **304–306** 362
[13] Kim Y H, Inoue A and Masumoto T 1990 *Mater. Trans. JIM* **31** 747
[14] Perepezko J H, Hebert R J and Wilde G 2004 *Mater. Sci. Eng.* A **375–377** 171
[15] Pradell T, Cespo D, Clavaguera N and Clavaguera-Mora M T 1998 *J. Phys.: Condens. Matter* **10** 3833
[16] Jacovkis D, Xiao Y, Rodriguez-Viejo J and Clavaguera-Mora M T 2004 *Acta Mater.* **52** 2819
[17] Clavaguera-Mora M T, Clavaguera N, Crespo D and Pradell T 2002 *Prog. Mater. Sci.* **47** 559
[18] Kissinger H E 1957 *Anal. Chem.* **29** 1702
[19] Kolmogorov A N 1937 *Izv. Akad. Nauk SSSR. Ser. Mater.* **1** 335
[20] Johnson W A and Mehl K E 1939 *Trans. Am. Inst. Min. Met. Eng.* **195** 416
[21] Avrami M 1939 *J. Chem. Phys.* **7** 1103
[22] Avrami M 1940 *J. Chem. Phys.* **8** 212
[23] Avrami M 1941 *J. Chem. Phys.* **9** 177
[24] Christian J W 1981 The theory of transformations in metals and alloys *Materials Science and Technology* (Oxford: Pergamon)